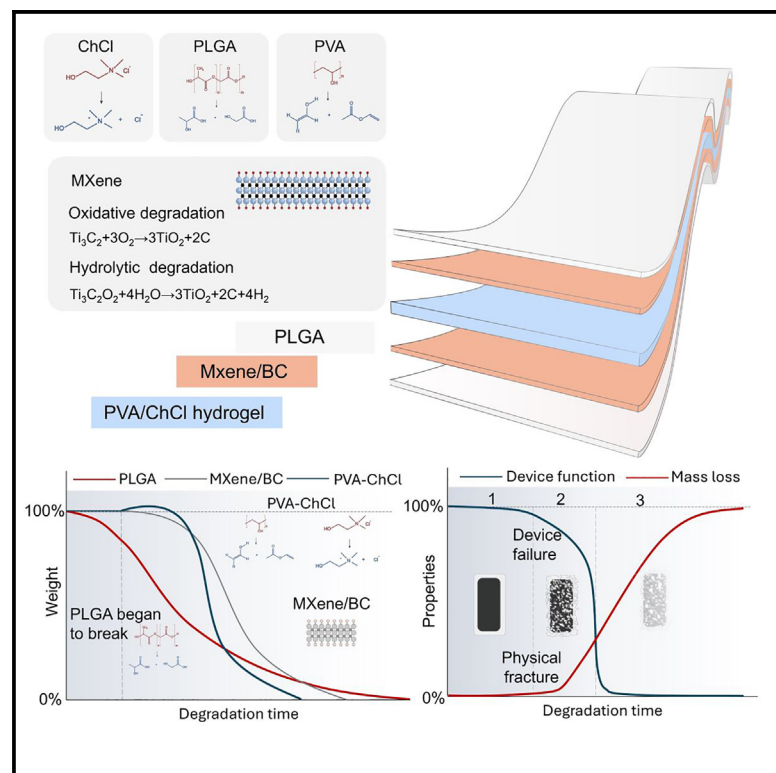


Symbiotic biodegradable flexible supercapacitor *in vivo*

Graphical abstract



Highlights

- A fully biodegradable supercapacitor to power implantable devices
- The 2D MXene electrode achieves excellent electrochemical performance
- The regulation of excitability and inhibition of rat nerves was realized

Authors

Engui Wang, Maosheng Wu, Lin Luo, ..., Wei Hua, Zhou Li, Han Ouyang

Correspondence

zli@binn.cas.cn (Z.L.),
ouyanghan@ucas.ac.cn (H.O.)

In brief

Biodegradable electronics dissolve *in vivo*, eliminating retention risks, but they are often not self-contained due to limited energy storage, relying typically on tethered or wireless power. We present a fully biodegradable flexible supercapacitor that is composed of MXene electrodes and solid electrolytes, which can be completely dissolved, is symbiotic with the body and can regulate nerve excitation and inhibition without external energy. These advancements are poised to drive the development of self-contained, biodegradable, and symbiotic bioelectronics.



Develop

Prototype with demonstrated applications in relevant environment

Wang et al., 2025, Device 3, 100724
June 20, 2025 © 2025 The Author(s). Published by Elsevier Inc.
<https://doi.org/10.1016/j.device.2025.100724>

CellPress

Article

Symbiotic biodegradable flexible supercapacitor *in vivo*

Engui Wang,^{1,2,6} Maosheng Wu,^{1,2,6} Lin Luo,^{1,6} Xi Cui,² Lingling Xu,² Ruizeng Luo,² Yang Zou,² Tian Le,¹ Yizhu Shan,² Yichang Quan,² Yuan Bai,² Li Wu,² Yiran Hu,⁵ Sijing Cheng,⁵ Juwei Yang,⁵ Chang Zhu,² Dengjie Yu,² Jianying Ji,² Yongfang Ren,¹ Dongjie Jiang,³ Bojing Shi,⁴ Hongqing Feng,^{1,2} Wei Hua,⁵ Zhou Li,^{1,2,*} and Han Ouyang^{1,2,7,*}

¹School of Nanoscience and Engineering, School of Chemical Sciences, University of Chinese Academy of Sciences, Beijing 100049, China

²Beijing Institute of Nanoenergy and Nanosystems, Chinese Academy of Sciences, Beijing 101400, China

³Department of Advanced Manufacturing and Robotics, College of Engineering, Peking University, Beijing 100871, China

⁴Key Laboratory for Biomechanics and Mechanobiology of Chinese Education Ministry, Beijing Advanced Innovation Centre for Biomedical Engineering, School of Biological Science and Medical Engineering, Beihang University, Beijing 100191, China

⁵Department of Cardiology, The Cardiac Arrhythmia Center, State Key Laboratory of Cardiovascular Disease, National Clinical Research Center of Cardiovascular Diseases, Fuwai Hospital, National Center for Cardiovascular Diseases, Chinese Academy of Medical Sciences and Peking Union Medical College, Beijing 100037, China

⁶These authors contributed equally

⁷Lead contact

*Correspondence: zli@binn.cas.cn (Z.L.), ouyanghan@ucas.ac.cn (H.O.)

<https://doi.org/10.1016/j.device.2025.100724>

THE BIGGER PICTURE Biodegradable electronic devices represent an emerging class of technology defined by the complete dissolution of a device in the body after completion of a prescribed operation to remove the hazards of device retention. This technique eliminates the need for a second removal procedure, thereby significantly reducing the financial burden of implanting the device on the patient as well as the risk of surgery. However, limited by the capacity of the energy storage element, biodegradable electronics, far from being self-sufficient, typically rely on tethers or wireless connections for transdermal power. To address this issue, this work reports on a biodegradable flexible supercapacitor (BFSC) that can be completely dissolved, enabling symbiosis with the human body and modulating neural excitation and inhibition without external energy. These advances are expected to facilitate the development of self-contained biodegradable and symbiotic bioelectronics.

SUMMARY

Biodegradable electronics dissolve *in vivo*, eliminating retention risks, but they are often not self-contained due to limited energy storage, relying on tethered or wireless power. Here, we report a biodegradable flexible supercapacitor (BFSC) that can be completely dissolved to achieve symbiosis with the body and modulate neural excitation and inhibition without external energy. Its low stiffness and favorable biocompatibility allow it to minimize interface mismatch and rejection to be integrated with the body like a biological tissue. The BFSC has a farad surface capacitance (0.36 F/cm^2), high energy density ($73.1 \mu\text{Wh/cm}^2$), and 1-month operating life *in vivo* due to the MXene nanolayered electrode and solid-state hydrogel electrolyte. The BFSC can drive bioelectric stimulation circuits to enable neuromodulation and cardiac pacing in rats and pigs. The scaffold-like BFSC almost completely inhibits neural activity. These advances are expected to facilitate the development of self-contained biodegradable and symbiotic bioelectronics.

INTRODUCTION

Electricity appears in every corner of an organism and controls communication, activities, and thinking.^{1–3} Bioelectronics can be used for therapeutic purposes by manipulating biological signals.^{4–10} Biodegradable devices are promising candidates for temporary therapies as they can be broken down into nutrients

that directly enter cells and tissues, thus avoiding long-term rejection or device-removal surgery. The mutual interaction of matter and energy between devices and living bodies enables them to evolve into symbiotic relationships.^{11–16} Biodegradable electronic devices (BEDs) have achieved great success in cardiac pacemaker neurostimulation and tissue repair.^{17–20} However, one of the long-standing challenges to BEDs is the lack

of an appropriate implantable power source.^{21–23} Reported BED power supply solutions include tether power or wireless power transfer^{18,22} and energy harvesters.²⁴ However, these devices have certain deficiencies. First, the cables of tether-powered devices need to pass through the skin and leave a persistent wound. Second, wireless-powered devices rely on external radiofrequency,^{18,22} light,^{20,25} or ultrasound waves¹⁷ through the skin and tissue to power them, limiting the depth and stability of BED implantation. Finally, energy harvester-powered devices need to be further improved in terms of stability and output power for biological signal manipulation. In addition, partial devices suffer from nonbiodegradability of some of their materials, mechanical rigidity, and relatively large form factors, which limit their use *in vivo*.

Self-contained devices with on-board power sources are expected to overcome the challenges of tethered or wireless devices and energy harvester-powered devices in terms of infection risk, stability, and output power.^{19,26–29} Recently, emerging biodegradable power sources have made great progress in primary cells and capacitors.^{19,21,30–35} However, current biodegradable power sources have struggled to meet the needs of a typical electronic device (pacemaker) for continuous operation during the perioperative period. This is due mainly to the limitations of the primary cell in terms of stability and the capacitor in terms of capacity. For example, biodegradable magnesium-based batteries have high energy density but uncontrolled discharges and a lifetime limited by Mg foil depletion (<1 week). Capacitors offer excellent cycling stability but are limited by energy density, mechanical rigidity, and the presence of partially nonbiodegradable materials.^{14,36,37} The result is reduced device service life and patient compliance because biodegradable power sources have limitations in capacity, lifetime, and softness. Therefore, fully biodegradable rechargeable high-capacity soft power sources are urgently needed.

Ti₃C₂T_x MXene as a class of multifunctional two-dimensional (2D) layered materials has become a research hotspot due to its superior properties such as simple preparation, high electrical conductivity, and good biosafety, all at the same time. Its biosafety has been demonstrated in various fields such as wound repair,³⁸ physiological signal monitoring,³⁹ photothermal therapy,⁴⁰ drug delivery,⁴¹ antimicrobial agents,⁴² and guided bone regeneration.⁴³ MXenes are characterized by high electrical conductivity and a large specific surface area, and they demonstrate favorable chemical stability within common electrolyte environments.⁴⁴ Owing to these remarkable properties, they have been extensively employed as electrode materials in the fabrication of supercapacitors.⁴⁵

We propose a fully biodegradable flexible supercapacitor (BFSC) with low stiffness and favorable biocompatibility to minimize interface mismatch and rejection that can be completely dissolved to achieve symbiosis with the body and modulate neural excitation and inhibition without external energy. The flexible supercapacitor has a farad level surface capacitance (0.36 F/cm²), high energy density (73.1 μWh/cm²), and high power density (1.2 mW/cm²). The BFSCs have a long cycle life (20,000 cycles) and a 1-month *in vivo* operating life (with a capacitance retention above 70%) with a high service efficiency¹¹ (25%); these were absorbed by the organism and completely

disappeared after 120 days. The biodegradable flexible supercapacitor can be closely integrated with the body like a biological tissue and drive bioelectric stimulation circuits, enabling neuromodulation and cardiac pacing proof-of-concept trials *in vivo* (rat and pig). This advancement represents a new path to extend the capacitance and stability of rechargeable biodegradable power sources.

RESULTS

Design of BFSC

The structure of symbiotic BFSCs mainly consists of electrodes, electrolytes, and encapsulation layers. Considering the softness and biosafety, the MXene (Tables S1 and S2),^{43,46} poly(vinyl alcohol) (PVA), choline chloride (ChCl), and poly(lactic-co-glycolic acid) (PLGA) are employed as the constituent materials of BFSCs. The electrode consists of MXene nanosheets and one-dimensional (1D) bacterial cellulose (BC). The 1D BC nanowires are inserted between densely stacked 2D MXene nanosheets to improve the layer spacing from about 1.29 to 1.55 nm to facilitate the transport of hydrated ions. The electrolyte consists of PVA hydrogel and ChCl, which is an edible salt with good biocompatibility and water solubility. The ChCl/PVA hydrogel electrolyte has the advantages of high salt concentration and good biosafety at the same time, which are conducive to reduce the self-discharge of BFSCs. The biodegradable soft PLGA was selected as the encapsulation layer of the BFSC due to its tunability, excellent biodegradability and biocompatibility, and its superior mechanical properties and processing flexibility (Figure 1A).^{47–50} After addressing a medical need, the BFSC is completely biodegradable to eliminate the hazards of device retention or the risks and costs associated with a secondary surgery for retrieval (Figure 1B).

Some envisioned use cases are illustrated in Figures 1C and 1D. BFSCs can modulate (stimulate/inhibit) nerves in living organisms. MXene/BC electrodes can be laser cut into defined sizes and shapes such as square, fork finger, and snake electrodes, making BFSCs more convenient for various *in vivo* application scenarios (Figures 1E–1G). Two BFSCs in series are enough to light up 40 light-emitting diodes (Figure 1H). This means they can power most bioelectronic devices and regulate the activity of biological tissues such as muscles and nerves. In addition, good softness of BFSCs allows them to maintain conformal and robust contact with curved and dynamically deforming organs. This is important to prevent unwanted mechanical damage to tissues and to ensure the stability of the operation of the implant.

MXene/BC electrodes and ChCl/PVA electrolytes

The MXene/BC electrodes were obtained by solution co-mingled filtration (Figures 2A, S1A, and S1B). MXene nanosheets were stacked together after filtration, and the multilayer structure increased the specific surface area and improved ion adsorption. The surface of the MXene/BC electrode is flat (Figure 2B). The chemical composition and structure were investigated using X-ray photoelectron spectroscopy (XPS), Raman spectroscopy, and X-ray diffraction (XRD). The Ti 2p high-resolution XPS spectra of the prepared Ti₃C₂ with peak deconvolution showed Ti-C 2p_{3/2} (455.01 eV), Ti-O-C 2p_{3/2} (455.78 eV), C-Ti-F 2p_{3/2}

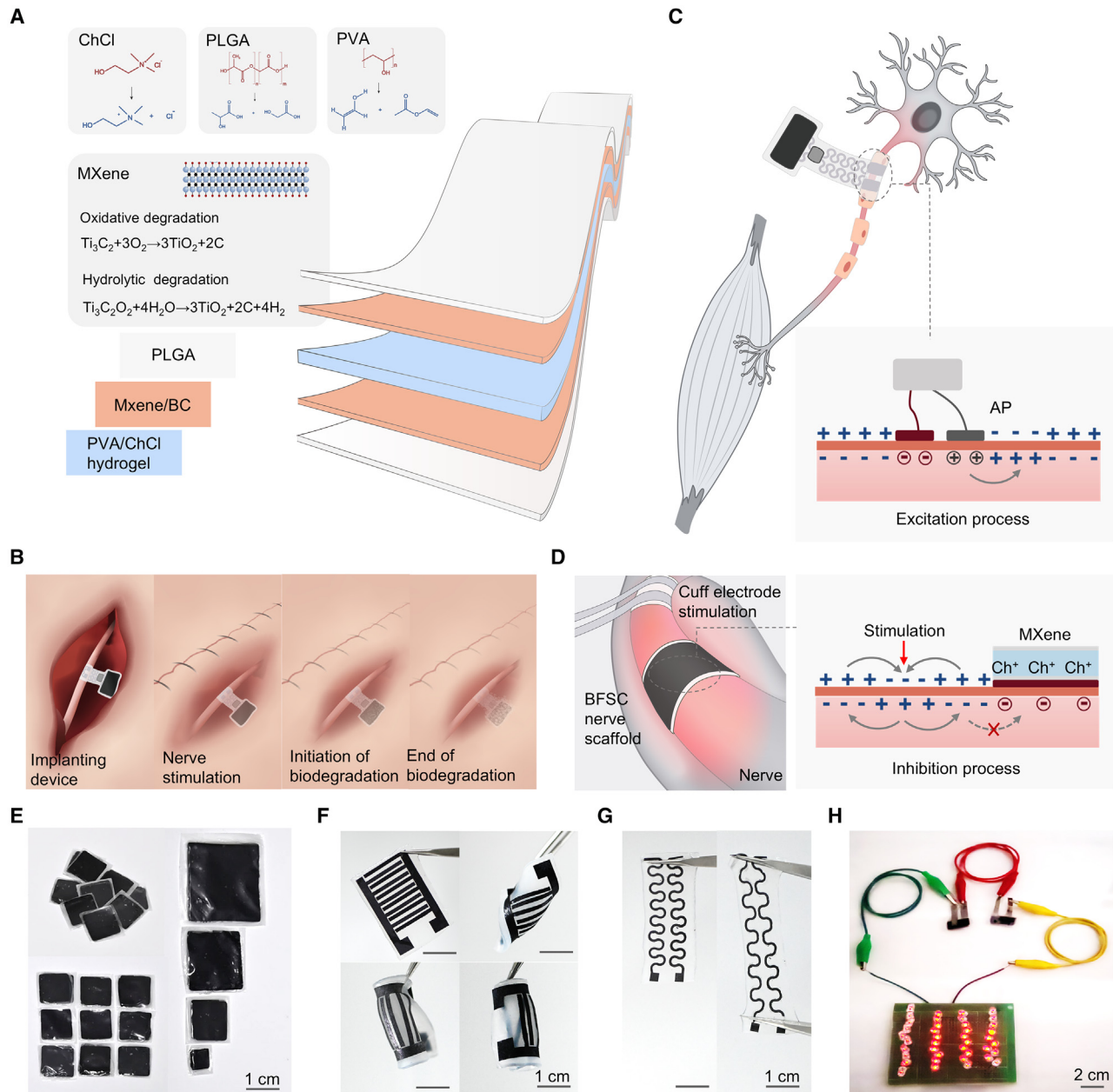


Figure 1. A fully BFSC for bioelectronics

(A) Schematic diagram of the structure, components, and *in vivo* degradation of a fully biodegradable flexible supercapacitor.

(B) Schematic of BFSC biodegradation.

(C) Schematic of BFSC neurostimulation.

(D) Schematic of BFSC neuroinhibition.

(E–G) BFSCs can be customized to different sizes and multiple morphologies.

(H) Application of BFSCs as an energy source for light-emitting diode lighting.

(456.91 eV), TiO₂ 2p_{3/2} (459.4 eV), Ti-C 2p_{1/2} (461.5 eV), and Ti-O-C 2p_{1/2} (462.25 eV), respectively (Figure 2C).⁵¹ This indicates that a small amount of TiO₂ is produced. Meanwhile, XPS and energy-dispersive X-ray spectroscopy (EDS) spectra reveal that the MXene electrode mainly contains Ti, O, and C elements (Figures 2, S1C, and S2). Raman spectra at the MXene/BC electrode

also demonstrated the synthesis of Ti₃C₂ (Figure 2E). BC is used as a spacer to increase the interlayer distance of MXene.⁵² The enlarged interspacing of the MXene/BC electrode compared with that of pristine MXene can be clarified through XRD measurements. According to the Bragg equation ($n\lambda = 2d \sin\theta$), when 1D BC nanowires are inserted between tightly stacked

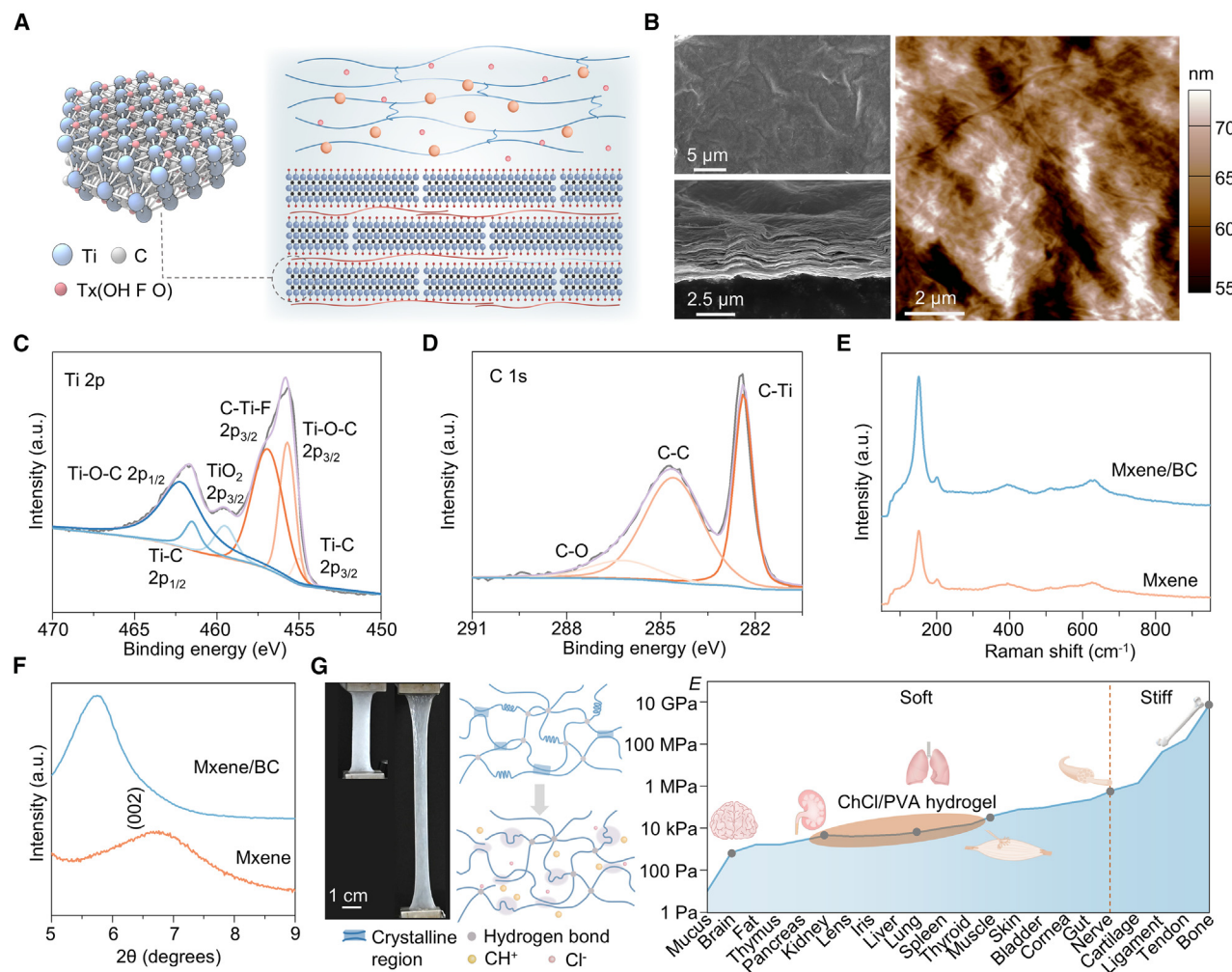


Figure 2. Characterization of MXene/BC electrode and ChCl-PVA hydrogel

(A) Atomic schematic of MXene.

(B) Top view and cross-sectional SEM image of MXene/BC electrode and AFM on the surface of MXene/BC electrode.

(C and D) XPS spectra covering Ti 2p (C) and O1s (D) orbitals.

(E) Raman spectra of MXene/BC electrode.

(F) XRD pattern of MXene/BC electrode.

(G) Schematic diagram of the fabrication process of ChCl-PVA hydrogel electrolyte, and the elastic moduli (E) of different tissues as described in the literature are reported on the left (logarithmic) scale.⁵³

MXene interlayers, the *d*-spacing values increased from about 1.29 to 1.55 nm ($2\theta = 6.8^\circ\text{--}5.7^\circ$) (Figure 2F). At the same time, BC was able to increase the mechanical strength of the MXene/BC electrodes (Figure S1D).

The electrolyte is a critical component of supercapacitors and influences their electrochemical performance.^{45,54} For implantation safety purposes, hydrogel is employed as the solid electrolyte for supercapacitors to prevent potential leakage of liquid fillers, internal short circuits, and other issues. The solid electrolyte should be small and thin and flexible/stretchable with high ionic conductivity. Additionally, good biocompatibility and biodegradability are also essential factors. In this system, the hydrogel electrolyte is composed of PVA, ChCl, and long PVA chains with high mechanical strength, which serve as the back-

bone of the polymer network (Figure 2G). The results of Fourier transform infrared spectroscopy (FTIR), Raman, and stress-strain tests show that ChCl/PVA hydrogels have good mechanical properties and flexibility and are well suited to BFSCs (Figures S1E and S1G). The performance of ChCl/PVA hydrogel electrolytes with different concentrations was studied. As the ChCl content increased, the volume of the PVA hydrogel also increased, mainly due to the strong hydration effect of the ions produced by the dissolution of the salt. These hydrated ions disrupted the original hydrogen bond network structure of the PVA hydrogel, allowing more free water to enter the hydrogel network, thus increasing its volume. After freeze-thaw cycles, the hydrogel volume decreases due to the Hofmeister effect,⁵⁵ which causes salting-out and electrostatic interactions, resulting

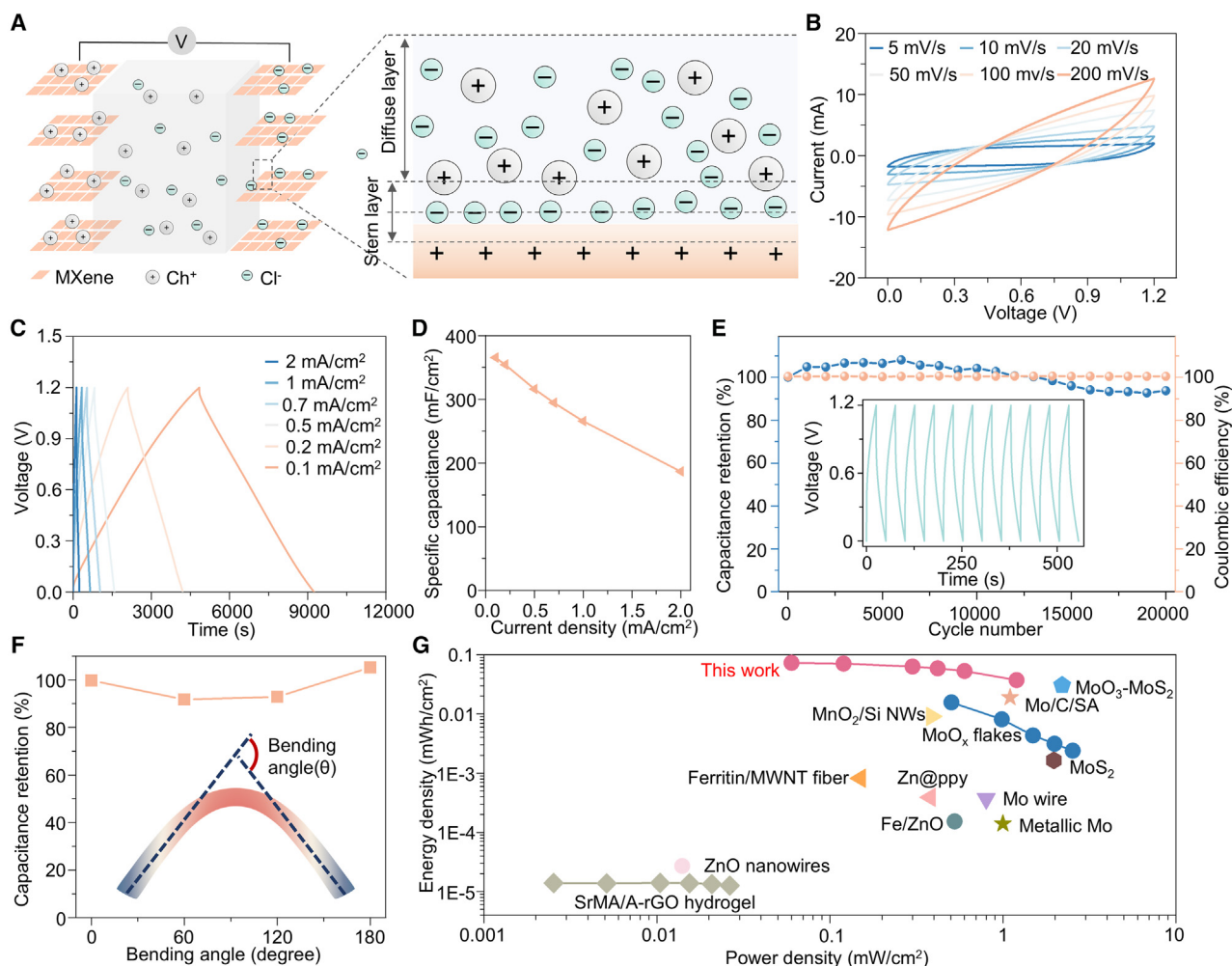


Figure 3. Electrochemical performance of MXene-based supercapacitors

- (A) Schematic illustration of the principle and structure of supercapacitors.
 (B) Cyclic voltammetry curves.
 (C) Galvanostatic charge-discharge curves.
 (D) Specific capacitances at different current densities.
 (E) Cycle stability and Coulombic efficiency curves.
 (F) Capacitance retention under different bending states of the supercapacitors using 36- μm MXene electrodes.
 (G) Ragone plots of the supercapacitor compared with other reported ones.

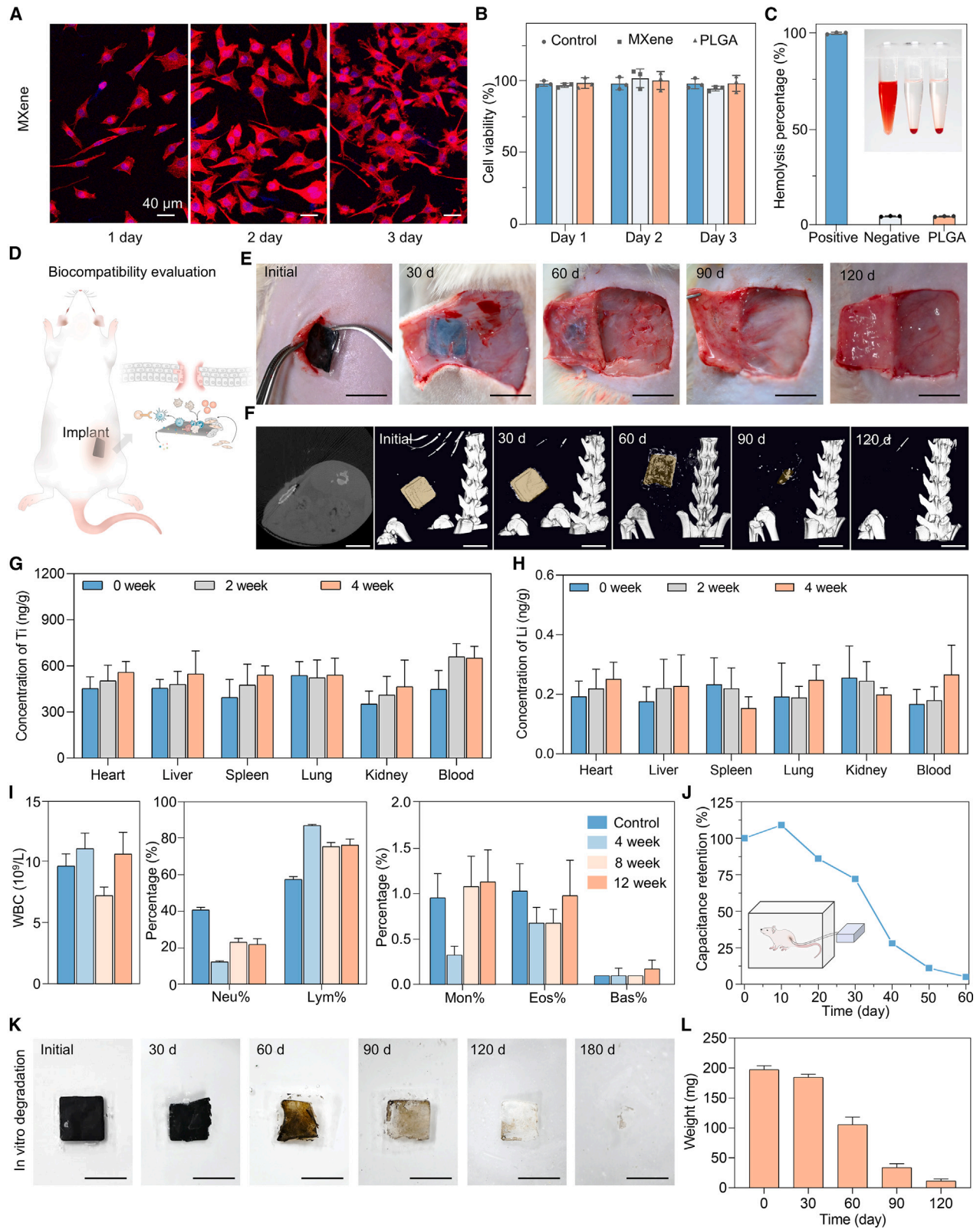
in a reduction in free water content within the hydrogel (Figure S3). The decrease in free water content in the hydrogel electrolyte helps suppress side reactions and improves the electrochemical performance of supercapacitors.

Study of the electrochemical properties of BFSCs

The BFSCs were assembled using MXene/BC electrodes with varying thicknesses and PVA hydrogel electrolytes containing different salt concentrations (Figure 3A). Initially, different concentrations of ChCl salts were introduced into the PVA hydrogel electrolytes. The results show that BFSCs assembled with 3 m ChCl/PVA hydrogel electrolytes exhibit the low self-discharge rates and the low leakage currents (Figure S4). Moreover, the self-discharge performance of the 3 m ChCl/PVA BFSC were

also far superior to other BFSCs assembled using several common bioabsorbable electrolytes (NaCl/PVA hydrogel, sodium alginate hydrogel, phosphate-buffered saline [PBS]/PVA hydrogel) (Figures S5 and S6). In addition, the electrochemical performance of BFSCs with MXene electrodes ranging in thickness from 3 to 36 μm was evaluated. The results of the electrochemical tests indicate that areal specific capacitance and self-discharge improve with increasing thickness (Figures S7–S9).

For BFSCs assembled using 3 m ChCl-PVA hydrogel electrolyte and 36 μm MXene/BC electrodes, the cyclic voltammetry (CV) curves exhibited quasi-rectangular shape with a voltage window of 0–1.2 V at scan rates from 5 to 200 mV/s (Figure 3B), indicating a typical electric double-layer mechanism and



(legend on next page)

good capacitive behavior. The galvanostatic charge-discharge (GCD) curves of the BFSCs exhibited a quasi-triangular shape in the range of 0.1–2 mA/cm², indicating excellent rate performance of the BFSCs (Figures 3C and 3D). The cycling stability of the BFSCs was also evaluated, and the capacitance retention of the supercapacitor after 20,000 cycles at 5 mA/cm² was 93.8%, with the coulomb efficiency consistently exceeding 99%. Due to the excessive thickness of the electrodes and the low free water content in the hydrogel electrolyte, the electrolyte could not fully infiltrate the electrodes at the beginning of the cycle, and thus the cycle curve showed a mild climbing phenomenon (Figure 3E). Furthermore, after bending 180°, the capacitance of the BFSCs exhibited minimal loss in the bending stability tests (Figure 3F). Due to the excellent stress stability and flexibility of MXene,⁴³ its structure remains intact after bending, maintaining stable charge storage and efficient ion diffusion (Figures S10A and 10B). These characteristics collectively ensure that the BFSCs retain high capacitance and stability under mechanical stress. Finally, the energy density and power density of BFSCs reported in the literature were compared (Figure 3G). The BFSCs exhibited significantly higher energy density (73.1 μWh/cm²) and power density (1.2 mW/cm²) than recently reported degradable supercapacitors (Tables S3 and S4), such as Fe/ZnO, MoO₃, MnO₂/Si NWs, Zn@ppy, and others,^{56–63} demonstrating that the BFSCs offer distinct advantages, including a higher energy density, superior biodegradability, and reliable functionality over extended periods compared to other existing technologies.

Cytotoxicity assessment and biosafety assessment

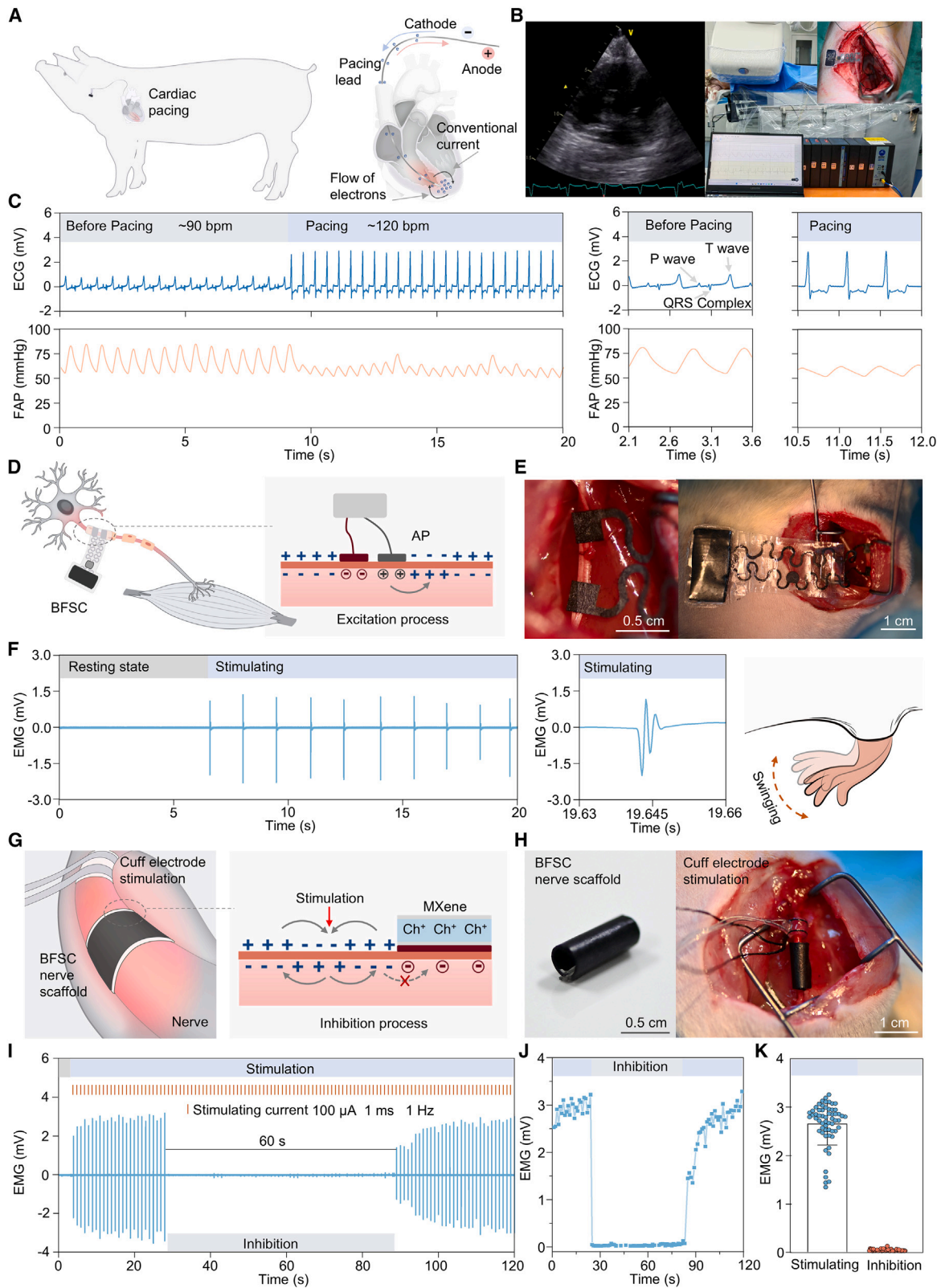
Biocompatibility is one of the basic requirements for implantable devices, which can be confirmed by determining the adhesion, proliferation, morphology, and cell viability of L929 cells grown on the surface of MXene/BC and PLGA films at different times (Figures S11 and S12) ($n = 3$). L929 cells showed good adhesion, spreading, and proliferation on the surface of MXene/BC and PLGA films (Figures 4A and S11). Subsequently, the same conclusion was reached by analyzing the results of the CCK-8 (Cell Counting Kit-8, $n = 3$) test, which demonstrated that cell viability remained above 96.4% after 3 days of growth (Figure 4B). Furthermore, the average hemolysis rate of PLGA and MXene/BC was significantly lower than the International Organization for Standardization standard (5%) (Figures 4C and S13) ($n = 3$). The preceding results demonstrated that all the materials that make up the supercapacitor were biocompatible and non-toxic, thereby ensuring the biosafety of the implanted BFSCs (Table S5).

BFSCs (1 × 1 cm) were implanted into the dorsal subcutis of Sprague-Dawley (SD) rats to assess their biodegradability and biosafety *in vivo*. The physical images of the BFSCs and the micro-computed tomography (micro-CT) images during degradation demonstrated that the device maintained its finished structure for 30 days and visibly degraded at 60 days. At 90 days, the PLGA and electrolytes were fully metabolized, and at 120 days, the device was completely degraded (Figures 4D–4F). This degradation process is significantly influenced by the biological environment, where high humidity, enzymatic activity, and biochemical interactions collectively accelerate the breakdown and support the efficient metabolic clearance of the degradation byproducts. The histology and biodistribution of MXene associated with biodegradability in a rat model reveal aspects related to toxicity. Figures 4G and 4H show the concentration of Ti and Li in the blood, heart, lung, liver, spleen, and kidney explants from SD rats at 2 and 4 weeks after MXene/BC implantation, measured by inductively coupled plasma-mass spectrometry (ICP-MS) (Figure S14). The organs of the control group and those with implanted MXene reveal no abnormal accumulation of Ti in the organs. There was no accumulation in the lungs. There is a small accumulation of Ti ions in the heart, liver, spleen, kidneys, and blood. At the same time, the control group and the organs implanted with MXene material showed no difference in Li in the organs and blood. The results of histological hematoxylin and eosin (H&E) staining of tissues in the vicinity of the implanted BFSCs and vital organs, in conjunction with the results of routine blood tests, simultaneously showed no significant difference from normal rats (Figures 4I, S15, and S16). The above results show that the degradation process does not cause toxicity and adverse effects on tissues and organs. MXene is degraded by oxidation and hydrolysis to form TiO₂ (Figure 1A),^{64,65} and in an *in vivo* environment, additional factors such as enzymes and reactive oxygen species (ROS) further affect the degradation process. Enzymes can accelerate Ti-C bond cleavage via hydrolysis, while ROS generated during inflammatory responses enhances oxidation, expediting MXene degradation.

The degradation of PLGA determines the service life of BFSCs, and due to its relatively low dissolution rate, the use of a ratio of 65:35 results in BFSCs remaining intact in the body and avoiding electrolyte leakage.⁴⁸ The *in vivo* operational stability of the BFSC was verified in a rat model (Figure 4J). At 30 days after BFSC implantation, the capacitance retention rate was 72%, but the capacitance retention of the BFSC decreased dramatically to 28% after 40 days and was almost capacitance-free at 60 days. *In vitro* degradation experiments in deionized water (75°C) revealed that by day 30, PLGA exhibited signs

Figure 4. Biosafety and biodegradability assessment of BFSCs

- (A) Immunofluorescent staining of L929 cells cultured on the surface of MXene/BC films. $n = 3$. Scale bar: 40 μm.
 (B) Percentage of cell viability of MXene/BC and PLGA film surface cells obtained by CCK-8 at 24, 48, and 72 h compared to controls ($n = 3$).
 (C) The result of the hemolysis ratio of the positive control, negative control, and PLGA group ($n = 3$).
 (D–F) *In vivo* degradation process of BFSC implants in the subcutaneous region of rat (D). Optical photographs (E) and CT images (F) of BFSCs at various stages of the degradation timeline in rats ($n = 3$). Scale bar: 1 cm.
 (G and H) *In vivo* distribution of key elements of ICP-MS ($n = 3$).
 (I) Routine blood of rats implanted with BFSCs at stages (4, 8, 12 weeks) ($n = 3$).
 (J) Subcutaneous electrochemical property changes in BFSC-implanted rats.
 (K and L) Image and quality loss of BFSCs at various stages of the degradation timeline (75°C, DI water, $n = 3$). Scale bar: 1 cm.



(legend on next page)

of degradation, leading to the exposure of the MXene and hydrogel electrolyte components to the solution environment. At 90 days, MXene was largely dissolved, leaving the hydrogel electrolyte and PLGA. After 180 days, all substances were basically dissolved (Figures 4K and 4L). Degradation experiments for each component demonstrate that all materials that make up the supercapacitors can degrade under different physiological conditions, with elevated temperatures accelerating the degradation process (Figures S17 and S18; Table S5).

BFSCs for bioelectrical stimulation

Here, we combined BFSCs with electronic components to construct an electrical stimulation system for therapy to demonstrate the immediate utility of using BFSCs as implantable biodegradable energy devices. The examples presented here include cardiac pacemakers (Figures 5A–5C) and neurostimulation/inhibition (Figures 5D–5K).

Pacemakers provide electrical stimulation therapy to address cardiac disorders.^{6,18} Temporary pacemakers are often used during the recovery period after cardiac surgery and use wires passed through the skin to connect to an external power source for stimulation. Thus, the BFSC-driven pacing circuit was subjected to testing (Figures 5A and 5B). The output electrical pulse stimulation generated by the pacing circuit can induce myocardial contraction and regulate heart rate. The heart rate increased from 90 beats per minute in the intrinsic phase to ~120 beats per minute in the effective pacing phase, and the systolic blood pressure decreased significantly from ~80 mm Hg in the intrinsic phase to ~60 mm Hg in the effective pacing phase due to the rapid pacing of the BFSCs (Figure 5C). The above results confirm that the BFSC-driven cardiac pacing systems can successfully realize cardiac pacing on a large animal scale. Due to current technical limitations, non-biodegradable pacemaker chips are used. However, the majority of the pacemaker system is made from biodegradable materials, significantly reducing the long-term burden of non-biodegradable components while maintaining reliable pacing function.

The biodegradable electrical stimulation system consists of a BFSC, a biodegradable pressure switch, and a biodegradable flexible circuit (Figures 5D and 5E). The bioabsorbable pressure switch consists of two conductive films and a spacer layer, which collectively regulate the generation of electrical signal pulses. The stimulation effect of a BFSC-based biodegradable electrical stimulation system was verified in a rat model. In our demonstration, the electrical stimulation electrodes were placed around the sciatic nerve. The MXene electrode is more hydrophilic after plasma treatment (Figure S19) and can be attached

securely to the sciatic nerve surface. The stimulation system was made to generate a pulse signal to stimulate the nerve by pressing the pressure switch by hand (the electromyogram [EMG] signals during the stimulation were recorded by a physiological recorder) (Figures 5E and 5F). As expected, the bioabsorbable electrical stimulation system generated electrical signals, which led to the elevation of the hindlimb (Video S1).

Notably, BFSCs also inhibit nerve signal transmission (Figure 5G). The positive charge of the BFSC neural scaffold induced a sustained negative charge on the surface of the nerve fiber membrane, which can suppress the conduction of positive charges, thereby blocking the transmission of nerve impulses from the proximal to the distal (Figures 5G and 5H). In this experiment, external stimulation of the electrode at the proximal nerve position (100 μ A, 1 ms, 1 Hz) continuously induced hindlimb movement, and the EMG was recorded by a physiological signal recorder. The BFSC scaffold was attached to the nerve, and after 60 s, the BFSC neural scaffold was removed. The BFSC neural scaffold could inhibit the transmission of the neural signals well (Figure 5I). Compared with the average EMG recorded without the BFSC neural scaffold, the BFSC neural scaffold could reduce the electrically evoked EMG by a relative 98% (Figure 5J). Statistical data are summarized and presented in Figures 5J and 5K. The achievement of such excellent performance can be attributed to the fact that 1) the BFSC nerve scaffold is ring shaped to encircle the nerve and is able to completely cover the circumference of the nerve fibers, and (2) the BFSC nerve scaffold is rated at 1.2 V, which is capable of inducing a high negative potential at the nerve-contacting interface to block the transmission of the electrical signals from the upper end stimulation electrode. Therefore, the BFSC nerve scaffold shows excellent peripheral nervous system inhibition ability.

DISCUSSION

In summary, we proposed a symbiotic biodegradable flexible supercapacitor, which showed excellent biodegradability and softness and was completely absorbed after being implanted subcutaneously in rats for 120 days. We used the emerging MXene material as capacitor electrodes and systematically demonstrated the biosafety and degradability of the devices. Meanwhile, BFSCs have excellent electrochemical properties (capacitance and energy density) and stability, surpassing previously reported biodegradable supercapacitors, with a surface capacitance of 0.36 F/cm² and an energy density of 73.1 μ Wh/cm². BFSCs have a long cycle life (20,000 cycles) and 1-month operating life *in vivo*, with high service efficiency (25%). BFSCs

Figure 5. BFSCs for bioelectrical stimulation

- (A) Schematic diagram of cardiac pacing lead connected to a BFSC for cardiac pacing.
- (B) Images of animal cardiac pacing.
- (C) Blood pressure and ECG before and after cardiac pacing stimulation.
- (D) Schematic diagram of peripheral nerve stimulation.
- (E) Image of BFSC bioresorbable electrical stimulation system.
- (F) EMG signals recorded during stimulation.
- (G) Principle of the inhibition process.
- (H) Images of BFSC-based neural scaffolds for the inhibition of peripheral neural activities experiments.
- (I–K) EMG signaling with and without BFSC-based neural scaffolds under external electrical stimulation.

can drive cardiac pacing, brain stimulation, and neurostimulation circuits, realizing heart stimulation in pigs and nerve stimulation in rats. Furthermore, they can function independently as a BED, effectively inhibiting nerve signal transmission in rats. This advancement offers new opportunities for improving the capacitance and stability of biodegradable capacitors. Looking ahead, we envision integrating BFSCs with other biodegradable energy-harvesting devices, such as triboelectric nanogenerators or wireless power transmission systems, to create fully integrated biodegradable electrostimulation systems. This would enable the development of self-power, long-term bioelectronic devices, advancing the field of biodegradable electronics and broadening their application in implantable therapeutic systems.

METHODS

Materials

Ti₃AlC₂ powder was purchased from 11 Technology. PVA (1799), choline chloride (ChCl, analytical reagent [AR]), and lithium fluoride (LiF, AR) were purchased from Aladdin. PLGA (65:35 [lactide:glycolide]) was purchased from Jinan Daigang Biomaterial. Concentrated hydrochloric acid (HCl, 36.5%) and dichloromethane (DCM; 99.8%) were purchased from Macklin. BC fibers were purchased from Guilin Qihong Technology.

Materials synthesis and preparation

The MXene materials were prepared using the following method: (1) etching: 5 mL of deionized (DI) water was added to 15 mL of 36%–38% HCl to prepare solution A. Then, 1 g of LiF and 1 g of MAX phase (Ti₃AlC₂) were dissolved in solution A to obtain solution B, which was stirred at 40°C for 24 h. (2) 20 mL of solution B was mixed with 15 mL of DI water to prepare solution C. Subsequently, solution C was centrifuged at 3,500 rpm for 3 minutes. Then, discard the supernatant, rinse with 35 mL DI water and centrifuge again. Repeat this step until the pH value of the supernatant drops to 6.0, and the precipitate is obtained. (3) Finally, the precipitate was diluted with DI water and treated with ultrasound in an ice bath for 1 h. Then, it was centrifuged at 3,500 rpm for 60 min to obtain a dispersed single-layer Ti₃C₂T_x nanosheet.

The MXene/BC electrode was prepared by vacuum filtration of the mixed solution, which was obtained by thoroughly stirring MXene and BC in a 9:1 mass ratio. MXene/BC electrodes with varying thicknesses were obtained by changing the quality of the solution. The ChCl/PVA hydrogel was fabricated through a one-pot and freezing-thawing method. Briefly, 1.0 g PVA and different molar concentrations of ChCl were dissolved in 9 mL DI water to form a homogeneous solution in a 95°C water bath with vigorous stirring for 1–2 h. Then, the uniform solution was molded into film by a glass mold, frozen at –80°C overnight, and transferred to room temperature for 6 h. This was repeated twice. The PLGA encapsulated film was prepared by the solvent evaporation method. Briefly, 1 g PLGA powder was dissolved into 10 mL DCM, and smooth PLGA film was obtained by spin coating (1,000 rpm).

Preparation of BFSCs

The MXene/BC film and ChCl/PVA hydrogel were cut into pieces (1 × 1 cm in area). Two MXene/BC electrodes were

covered on the upper and lower surfaces of the hydrogel electrolyte. Finally, the as-fabricated BFSC was set between two PLGA layers. Then, the PLGA solution at high concentration (10%, w/v) was used as an adhesive to carefully stick together the edges of the two PLGA layers. The device was air dried for 12 h and further sealed by a heat sealer to exclude any interstice and ensure that the BFSC was protected from the environment.

Characterization measurements

The morphology of the top surface, bottom surface, and cross-section of the MXene/BC films and related elemental information was characterized by scanning electron microscopy (SEM) and EDS (NOVA450). The surface and height of the sample were detected by atomic force microscopy (AFM) using a Dimension ICON system (Bruker). The chemical composition and state of MXene/BC films were measured by X-ray photoelectron spectroscopy (XPS) with a Thermo ESCALAB 250 instrument. FTIR was obtained using a VERTEX80v spectrometer (Bruker). Crystal and elementary compositions were analyzed by XRD, which was performed using PANalytical X'Pert3 Power with 2θ ranging from 5° to 10°, where Cu Kα radiation (λ = 1.5406 Å) was operated at 40 kV and 40 mA and Raman spectra were equipped with an Ar laser working at a wavelength of 532 nm (LabRAM HR Evolution, Horiba) at room temperature. The tensile test of the hydrogel was performed using the ESM301/Mark-10 system at room temperature.

Electrochemical measurements

The MXene/BC films were then cut into circle shapes of 12-mm diameter. Two-electrode cells were assembled using MXene/BC electrodes and ChCl/PVA hydrogel to form symmetric supercapacitors. The thicknesses of MXene/BC electrodes were 3, 6, 9, 12, 24, and 36 μm, respectively. CV, GCD, and electrochemical impedance spectroscopy tests were obtained using an electrochemical workstation (CHI660E). Self-discharge curves and leakage currents were obtained from a battery tester system (Arbin BT2000).

The areal capacitances (C) of the cells were obtained from GCD curves:

$$C = \frac{It}{sV} \quad (\text{Equation 1})$$

where I is the discharge current of the supercapacitors, t is the discharge time, s is the area of a single electrode, and V is the voltage window.

The specific energy densities (E) of the cells can be evaluated with the following equation:

$$E = \frac{CV^2}{2 * 3600} \quad (\text{Equation 2})$$

The power density (P) of the cells can be evaluated with the following equation:

$$P = \frac{E * 3600}{t} \quad (\text{Equation 3})$$

The BFSC service efficiency parameter is defined in the following equation:

$$\text{Service efficiency} = \frac{\text{operational lifetime}}{\text{degradation time}} \quad (\text{Equation 4})$$

Operational lifetime is the period during which the device retains at least 70% of its initial capacitance, and degradation time is the time required for the complete degradation of the device.

Cell biocompatibility and proliferation evaluations

L929 cells are widely used as biocompatibility test materials because of their stable growth characteristics, rich research data, and good representativeness, and they are easy to obtain and culture. L929 cells were cultured with standard Dulbecco's modified Eagle's medium (DMEM, Gibco) supplemented with 1% penicillin-streptomycin (Gibco) and 10% fetal bovine serum (Gibco) at 37°C in a 5% CO₂ atmosphere, and the medium was replaced every 2 days. The biocompatibility of the materials was tested by a live/dead assay (Solarbio). Samples of different materials weighing 10 mg were first soaked in 20 mL DMEM for 24 h, and the leachate was retained. Cells were incubated in the leachate for 3 days and then stained with live/dead assay according to the reagent vendor's instructions ($n = 3$). Briefly, the cell samples were incubated with the prepared solution at 37°C for 20 min and then observed using a fluorescence microscope (DMI 6000). Furthermore, the cell proliferation level for 1, 2, and 3 days was evaluated by a CCK-8 assay (Solarbio). Specifically, following the removal of the medium and the washing of the cell samples with PBS, the samples were incubated with medium containing 10% CCK-8 reagent. After incubation at 37°C for 1.5 h, absorbance at 450 nm was measured using a microplate reader (Thermo Fisher Scientific).

Cell morphology and immunofluorescent staining

Cell morphology can show the state of cell growth on different substrates. The cytoskeleton and nucleus were stained with phalloidin (Abcam) and 4',6-diamidino-2-phenylindole (DAPI, Solarbio). The L929 cells were cultured on the surface of different material films ($n = 3$) for 1, 2, and 3 days to observe cell morphology. Before staining, the cells were fixed with 4% paraformaldehyde (Solarbio) for 10 min and permeabilized with 0.1% Triton X-100 (Solarbio) for 5 min. Finally, the cells were stained with phalloidin for 30 min and DAPI for 10 min at room temperature and washed three times with PBS. The stained cells were then visualized using a laser scanning confocal microscope (SP8, Leica, Germany).

Hemolysis assay

The fresh blood (1 mL) of rats (male, 6 weeks old, 200 g) was taken into an anticoagulant tube, and the supernatant was removed after 2 mL PBS (Solarbio) was washed 5 times (1,000 rpm, 5 min). The washed red blood cells were resuspended by 10 mL PBS (Solarbio) as the blood working solution. The material group consisted of 200 μ L of blood working solution and 800 μ L of material leached solution, which was prepared by immersing 1 mg of PLGA film and MXene/BC film in 1 mL of

normal saline for 3 days. The positive group ($n = 3$) received 200 μ L of blood working solution and 200 μ L of water, while the negative group ($n = 3$) received 200 μ L of blood working solution and 200 μ L of PBS. After incubating at 37°C for 4 h, the mixture was centrifuged in at 1000 rpm for 5 min and photographed for recording, and 100 μ L of the supernatant samples from each group were used to test the absorbance at 577 nm.

In vitro degradation evaluation

Regarding compositional degradation, PLGA, MXene/BC, and PVA/ChCl were cut into 1 \times 1 cm sizes and immersed in Petri dishes containing 1 \times PBS and DMEM with high glucose, respectively, and heated to 60°C/37°C on a hot plate ($n = 3$). The solution in the Petri dishes was changed every day. The BFSCs were immersed in a Petri dish containing DI water and heated to 70°C on a hot plate ($n = 3$) to degrade the device. The DI water in the Petri dish was replaced daily. Time series images were captured at various stages using a Nikon D780 camera.

In vivo degradation evaluation

Before surgery, the SD rats underwent a one-week acclimatization period. The BFSCs were sterilized with ultraviolet light and 75% alcohol for 1 h and then implanted subcutaneously into the backs of the rats. The backs of the SD rats were opened at different time periods to observe the degradation of the BFSCs, and photographs were taken with a Nikon D780 camera. BaSO₄ with a mass fraction of 10% was added to the BFSCs as a developer, and *in vivo* degradation was assessed by micro-CT. The rats were euthanized at different time intervals after implantation of the BFSCs, and histological analysis (H&E staining) was performed on the tissues and organs surrounding the implanted devices ($n = 3$). For the blood routine examination ($n = 3$), tail vein blood of the rats was collected and stored in anticoagulant blood collection vessels, and then the levels of inflammatory cells in the blood were evaluated by using an animal blood cell analyser (52VET, Beijing Keyue Huacheng Technology).

ICP-MS study

MXene/BC (1 \times 1 cm) was disinfected with ultraviolet light and 75% alcohol for 1 h and implanted subcutaneously into the backs of SD rats. MXene solution (10 mg/mL) was injected subcutaneously (10 mg kg⁻¹) in SD rats. After the material was implanted, the rats were euthanized at different intervals and blood and tissue were taken. The Ti and Li content of the test sample was measured by ICP-MS (Thermo *iCAP Q*). Different tissues of the rats were excised for ICP-MS detection, the tissues were transferred to glass bottles, and then they were digested overnight in HNO₃. Next, they were heated to 180°C and kept there for 1 h, and H₂O₂ was added until the sample was fully digested. Next, the solution was heated to 260°C to remove any remaining HNO₃. Finally, the remaining colorless solution was diluted to 3 mL with 2% HNO₃ and analyzed by ICP-MS.

In vivo study—electrochemical measurements

Before surgery, the animals underwent a one-week acclimatization period (female, 8 weeks old, 180 g). To measure the electrochemical performance of BFSCs *in vivo*, we implanted the capacitor in the dorsal subdermal region of an SD rat where

operation and observation are more convenient. A transparent sterile occlusive dressing, Tegaderm (3M), was then placed over the wound and the lead wires (Figure S20). This can effectively prevent the lead wire from being scratched by the rats. The electrochemical performance of BFSCs was tested every 10 days using an electrochemical workstation (CHI660E).

In vivo study—neurostimulation/inhibition

SD rats (female, 8 weeks old, 180 g) were deeply anesthetized with pentobarbital sodium (60–80 mg kg⁻¹). The sciatic nerve was exposed without muscle damage by releasing the surrounding connective tissue. In the stimulation experiments, electrical stimulation electrodes were placed around the sciatic nerve, and the stimulation system was made to generate a pulsed signal to stimulate the nerve by pressing a pressure switch by hand. During inhibition experiments, another stimulating electrode (cuff electrode, KedouBC) positioned at the proximal site of the nerve evoked compound muscle action potentials, with a frequency of 1 Hz, a pulse current of 100 μ A, and a pulse width of 1 m (STG 4008, MCS Stimulus Generators). The BFSC neural scaffold was placed below the stimulating electrode. The electrophysiological recorder (Biopac MP150) was used to record the EMG, the pair of electrodes was inserted into the subcutaneous tissue near the foot muscles, and the ground electrode was placed under the skin away from the measurement site.

Porcine model of cardiac pacing

The BFSCs drive the pacing chip and connect the pacing lead for cardiac pacing. First, the skin of the right side of the neck was prepared with a tincture of iodine solution. Second, the external jugular vein was exposed with a small incision, and the pacing lead was implanted through the external jugular vein and advanced across the tricuspid valve. The lead was deployed at the right ventricular apex. The electrophysiological recorder (Biopac MP150) was used to record the electrocardiogram (ECG) and femoral artery pressure. The study protocol was approved by the State Key Laboratory of Cardiovascular Disease and Fuwai Hospital (ethical approval no. 0104-1-4-ZX(X)-23).

Animal experiments

All rat experiments were performed according to protocols approved by the Committee on Ethics of the Beijing Institute of Nanoenergy and Nanosystems (2023016LZ), and all animal procedures were carried out in line with the national standards of the Laboratory Animal Requirements of Environment and Housing Facilities (GB14925-2001).

Statistical analysis

All experiments were repeated at least three times. Data were analyzed as mean \pm standard deviation. Origin 2021 and GraphPad Prism version 8.0. were used for data analysis and plotting.

RESOURCE AVAILABILITY

Lead contact

Further information and requests for resources should be directed to and will be fulfilled by the lead contact, Han Ouyang (ouyanghan@ucas.ac.cn).

Materials availability

This study did not generate new unique reagents.

Data and code availability

All data supporting this study and its findings are available within the article and its [supplemental information](#) or from the corresponding author upon reasonable request.

ACKNOWLEDGMENTS

This project is supported by National Key Research and Development Program of China grant no. 2023YFC2411901 (to H.O.); National Natural Science Foundation of China grant nos. 52373256 (to H.O.), T2125003 (to Z.L.), and 62004010 (to H.O.); Youth Innovation Promotion Association CAS grant no. 2023176 (to H.O.); Beijing Natural Science Foundation grant nos. 7232347 (to H.O.) and L212010 (to Z.L.); the Beijing Nova Program grant 2024047 (to H.O.); and Fundamental Research Funds for the Central Universities grant nos. E0EG6802X2 (to Z.L.) and E2E45101X2 (to H.O.). We are [very grateful to Prof. Xianmao Lu (Beijing Institute of Nanoenergy and Nanosystems, BINN) for his insightful and detailed suggestions on project conception and capacitor theory. The authors appreciate the members of the State Key Laboratory of Cardiovascular Disease of the China Research Facility for their help in animal experiment surgery and postoperative care, as well as the members of the BINN and University of Chinese Academy of Sciences research facilities for their help in microfabrication/characterization.

AUTHOR CONTRIBUTIONS

H.O. and Z.L. conceived and coordinated the project and experiments. E.W., M.W., D.J., and B.S. assisted in concept development, sample preparation, and manuscript writing. E.W., Y.B., and J.J. conducted the materials preparation and characterization. E.W., M.W., C.Z., T.L., and Y.Z. conducted the electrochemical testing. X.C., R.L., and Y.S. conducted the cell experiment. E.W., L.X., L.W., Y.R., and D.Y. conducted the *in vivo* animal experiments (SD rats). W.H. directed and Y.H., S.C., E.W., and L.L. conducted the *in vivo* animal experiments (pig). E.W., Y.C.Q., and C.Z., conducted the *in vivo* animal experiments. E.W., M.W., L.L., and X.C. processed the data and drew the figures. E.W., M.W., and H.O. wrote the paper. H.O. and Z.L. directed the project. All authors read and revised the manuscript.

DECLARATION OF INTERESTS

The authors declare no competing interests.

SUPPLEMENTAL INFORMATION

Supplemental information can be found online at <https://doi.org/10.1016/j.device.2025.100724>.

Received: November 2, 2024

Revised: January 17, 2025

Accepted: February 5, 2025

Published: March 6, 2025

REFERENCES

- Li, J., Xu, Y., and Gao, W. (2024). Injectable and retrievable soft electronics. *Nat. Mater.* 23, 591–593. <https://doi.org/10.1038/s41563-024-01877-1>.
- Shi, J., Kim, S., Li, P., Dong, F., Yang, C., Nam, B., Han, C., Eig, E., Shi, L.L., Niu, S., et al. (2024). Active biointegrated living electronics for managing inflammation. *Science* 384, 1023–1030. <https://doi.org/10.1126/science.adl1102>.
- Yin, J., Wang, S., Tat, T., and Chen, J. (2024). Motion artefact management for soft bioelectronics. *Nat. Rev. Bioeng.* 2, 541–558. <https://doi.org/10.1038/s44222-024-00175-4>.

- Someya, T., Bao, Z., and Malliaras, G.G. (2016). The rise of plastic bioelectronics. *Nature* 540, 379–385. <https://doi.org/10.1038/nature21004>.
- Deng, J., Yuk, H., Wu, J., Varela, C.E., Chen, X., Roche, E.T., Guo, C.F., and Zhao, X. (2021). Electrical bioadhesive interface for bioelectronics. *Nat. Mater.* 20, 229–236. <https://doi.org/10.1038/s41563-020-00814-2>.
- Ouyang, H., Liu, Z., Li, N., Shi, B., Zou, Y., Xie, F., Ma, Y., Li, Z., Li, H., Zheng, Q., et al. (2019). Symbiotic cardiac pacemaker. *Nat. Commun.* 10, 1821. <https://doi.org/10.1038/s41467-019-09851-1>.
- Wang, T., Ouyang, H., Luo, Y., Xue, J., Wang, E., Zhang, L., Zhou, Z., Liu, Z., Li, X., Tan, S., et al. (2024). Rehabilitation exercise-driven symbiotic electrical stimulation system accelerating bone regeneration. *Sci. Adv.* 10, eadi6799. <https://doi.org/10.1126/sciadv.adi6799>.
- Kathe, C., Skinnider, M.A., Hutson, T.H., Regazzi, N., Gautier, M., Demesmaeker, R., Komi, S., Ceto, S., James, N.D., Cho, N., et al. (2022). The neurons that restore walking after paralysis. *Nature* 611, 540–547. <https://doi.org/10.1038/s41586-022-05385-7>.
- Ren, Y., Zhang, F., Yan, Z., and Chen, P.-Y. (2025). Wearable bioelectronics based on emerging nanomaterials for telehealth applications. *Device* 3, 100676. <https://doi.org/10.1016/j.device.2024.100676>.
- Traverso, G., Finomore, V., Jr., Mahoney, J., III, Kupec, J., Stansbury, R., Bacher, D., Pless, B., Schuetz, S., Hayward, A., Langer, R., and Rezaei, A. (2023). First-in-human trial of an ingestible vitals-monitoring pill. *Device* 1, 100125. <https://doi.org/10.1016/j.device.2023.100125>.
- Ouyang, H., Li, Z., Gu, M., Hu, Y., Xu, L., Jiang, D., Cheng, S., Zou, Y., Deng, Y., Shi, B., et al. (2021). A Bioresorbable Dynamic Pressure Sensor for Cardiovascular Postoperative Care. *Adv. Mater.* 33, 2102302. <https://doi.org/10.1002/adma.202102302>.
- Shan, Y., Wang, E., Cui, X., Xi, Y., Ji, J., Yuan, J., Xu, L., Liu, Z., and Li, Z. (2024). A Biodegradable Piezoelectric Sensor for Real-Time Evaluation of the Motor Function Recovery After Nerve Injury. *Adv. Funct. Mater.* 34, 2400295. <https://doi.org/10.1002/adfm.202400295>.
- Cui, X., Xu, L., Shan, Y., Li, J., Ji, J., Wang, E., Zhang, B., Wen, X., Bai, Y., Luo, D., et al. (2024). Piezocatalytically-induced controllable mineralization scaffold with bone-like microenvironment to achieve endogenous bone regeneration. *Sci. Bull.* 69, 1895–1908. <https://doi.org/10.1016/j.scib.2024.04.002>.
- Zhang, Y., Lee, G., Li, S., Hu, Z., Zhao, K., and Rogers, J.A. (2023). Advances in Bioresorbable Materials and Electronics. *Chem. Rev.* 123, 11722–11773. <https://doi.org/10.1021/acs.chemrev.3c00408>.
- Quan, Y., Wang, E., Ouyang, H., Xu, L., Jiang, L., Teng, L., Li, J., Luo, L., Wu, X., Zeng, Z., et al. (2024). Biodegradable and Implantable Triboelectric Nanogenerator Improved by β -Lactoglobulin Fibrils-Assisted Flexible PVA Porous Film. *Adv. Sci.* 2409914. <https://doi.org/10.1002/advs.202409914>.
- Li, S., Zhao, K., Zan, G., Kim, G., Oh, J., Jiang, W., Shin, E., Kim, W., Kim, T., Jang, J., et al. (2024). A biodegradable silk-based energy-generating skin with dual-mode tactile perception. *Device* 3, 100561. <https://doi.org/10.1016/j.device.2024.100561>.
- Lee, D.-M., Kang, M., Hyun, I., Park, B.-J., Kim, H.J., Nam, S.H., Yoon, H.-J., Ryu, H., Park, H.-m., Choi, B.-O., and Kim, S.-W. (2023). An on-demand bioresorbable neurostimulator. *Nat. Commun.* 14, 7315. <https://doi.org/10.1038/s41467-023-42791-5>.
- Choi, Y.S., Yin, R.T., Pfenninger, A., Koo, J., Avila, R., Benjamin Lee, K., Chen, S.W., Lee, G., Li, G., Qiao, Y., et al. (2021). Fully implantable and bioresorbable cardiac pacemakers without leads or batteries. *Nat. Biotechnol.* 39, 1228–1238. <https://doi.org/10.1038/s41587-021-00948-x>.
- Wu, H., Wang, Y., Li, H., Hu, Y., Liu, Y., Jiang, X., Sun, H., Liu, F., Xiao, A., Chang, T., et al. (2024). Accelerated intestinal wound healing via dual electrostimulation from a soft and biodegradable electronic bandage. *Nat. Electron.* 7, 299–312. <https://doi.org/10.1038/s41928-024-01138-8>.
- Huang, Y., Cui, Y., Deng, H., Wang, J., Hong, R., Hu, S., Hou, H., Dong, Y., Wang, H., Chen, J., et al. (2023). Bioresorbable thin-film silicon diodes for the optoelectronic excitation and inhibition of neural activities. *Nat. Biomed. Eng.* 7, 486–498. <https://doi.org/10.1038/s41551-022-00931-0>.
- Sheng, H., Zhou, J., Li, B., He, Y., Zhang, X., Liang, J., Zhou, J., Su, Q., Xie, E., Lan, W., et al. (2021). A thin, deformable, high-performance supercapacitor implant that can be biodegraded and bioabsorbed within an animal body. *Sci. Adv.* 7, eabe3097. <https://doi.org/10.1126/sciadv.abe3097>.
- Sheng, H., Jiang, L., Wang, Q., Zhang, Z., Lv, Y., Ma, H., Bi, H., Yuan, J., Shao, M., Li, F., et al. (2023). A soft implantable energy supply system that integrates wireless charging and biodegradable Zn-ion hybrid supercapacitors. *Sci. Adv.* 9, eadh8083. <https://doi.org/10.1126/sciadv.adh8083>.
- Zhou, J., Zhang, R., Xu, R., Li, Y., Tian, W., Gao, M., Wang, M., Li, D., Liang, X., Xie, L., et al. (2022). Super-Assembled Hierarchical Cellulose Aerogel-Gelatin Solid Electrolyte for Implantable and Biodegradable Zinc Ion Battery. *Adv. Funct. Mater.* 32, 2111406. <https://doi.org/10.1002/adfm.202111406>.
- Jiang, W., Li, H., Liu, Z., Li, Z., Tian, J., Shi, B., Zou, Y., Ouyang, H., Zhao, C., Zhao, L., et al. (2018). Fully Bioabsorbable Natural-Materials-Based Triboelectric Nanogenerators. *Adv. Mater.* 30, 1801895. <https://doi.org/10.1002/adma.201801895>.
- Li, P., Zhang, J., Hayashi, H., Yue, J., Li, W., Yang, C., Sun, C., Shi, J., Huberman-Shlaes, J., Hibino, N., and Tian, B. (2024). Monolithic silicon for high spatiotemporal translational photostimulation. *Nature* 626, 990–998. <https://doi.org/10.1038/s41586-024-07016-9>.
- Liu, R., Wang, Z.L., Fukuda, K., and Someya, T. (2022). Flexible self-charging power sources. *Nat. Rev. Mater.* 7, 870–886. <https://doi.org/10.1038/s41578-022-00441-0>.
- Kaveti, R., Jakus, M.A., Chen, H., Jain, B., Kennedy, D.G., Caso, E.A., Mishra, N., Sharma, N., Uzunoğlu, B.E., Han, W.B., et al. (2024). Water-powered, electronics-free dressings that electrically stimulate wounds for rapid wound closure. *Sci. Adv.* 10, eado7538. <https://doi.org/10.1126/sciadv.ado7538>.
- Zhang, Y., Tan, C.M.J., Toepfer, C.N., Lu, X., and Bayley, H. (2024). Micro-scale droplet assembly enables biocompatible multifunctional modular iontronics. *Science* 386, 1024–1030. <https://doi.org/10.1126/science.adr0428>.
- Cheng, P., Dai, S., Liu, Y., Li, Y., Hayashi, H., Papani, R., Su, Q., Li, N., Dai, Y., Liu, W., et al. (2024). An intrinsically stretchable power-source system for bioelectronics. *Device* 2, 100216. <https://doi.org/10.1016/j.device.2023.100216>.
- Li, H., Zhao, C., Wang, X., Meng, J., Zou, Y., Noreen, S., Zhao, L., Liu, Z., Ouyang, H., Tan, P., et al. (2019). Fully Bioabsorbable Capacitor as an Energy Storage Unit for Implantable Medical Electronics. *Adv. Sci.* 6, 1801625. <https://doi.org/10.1002/advs.201801625>.
- Lee, G., Kang, S.-K., Won, S.M., Gutruf, P., Jeong, Y.R., Koo, J., Lee, S.-S., Rogers, J.A., and Ha, J.S. (2017). Fully Biodegradable Microsupercapacitor for Power Storage in Transient Electronics. *Adv. Energy Mater.* 7, 1700157. <https://doi.org/10.1002/aenm.201700157>.
- Karami-Mosammam, M., Danninger, D., Schiller, D., and Kaltenbrunner, M. (2022). Stretchable and Biodegradable Batteries with High Energy and Power Density. *Adv. Mater.* 34, 2204457. <https://doi.org/10.1002/adma.202204457>.
- Huang, X., Hou, H., Yu, B., Bai, J., Guan, Y., Wang, L., Chen, K., Wang, X., Sun, P., Deng, Y., et al. (2023). Fully Biodegradable and Long-Term Operational Primary Zinc Batteries as Power Sources for Electronic Medicine. *ACS Nano* 17, 5727–5739. <https://doi.org/10.1021/acsnano.2c12125>.
- Tsang, M., Armutlulu, A., Martinez, A.W., Allen, S.A.B., and Allen, M.G. (2015). Biodegradable magnesium/iron batteries with polycaprolactone encapsulation: A microfabricated power source for transient implantable devices. *Microsyst. Nanoeng.* 1, 15024. <https://doi.org/10.1038/micronano.2015.24>.
- Yin, L., Huang, X., Xu, H., Zhang, Y., Lam, J., Cheng, J., and Rogers, J.A. (2014). Materials, Designs, and Operational Characteristics for Fully Biodegradable Primary Batteries. *Adv. Mater.* 26, 3879–3884. <https://doi.org/10.1002/adma.201306304>.

36. Chen, C., Zhang, Y., Li, Y., Dai, J., Song, J., Yao, Y., Gong, Y., Kierzewski, I., Xie, J., and Hu, L. (2017). All-wood, low tortuosity, aqueous, biodegradable supercapacitors with ultra-high capacitance. *Energy Environ. Sci.* *10*, 538–545. <https://doi.org/10.1039/C6EE03716J>.
37. Huang, I., Zhang, Y., Arafa, H.M., Li, S., Vazquez-Guardado, A., Ouyang, W., Liu, F., Madhupathy, S., Song, J.W., Tzavelis, A., et al. (2022). High performance dual-electrolyte magnesium–iodine batteries that can harmlessly resorb in the environment or in the body. *Energy Environ. Sci.* *15*, 4095–4108. <https://doi.org/10.1039/D2EE01966C>.
38. Li, Y., Fu, R., Duan, Z., Zhu, C., and Fan, D. (2022). Artificial Nonenzymatic Antioxidant MXene Nanosheet-Anchored Injectable Hydrogel as a Mild Photothermal-Controlled Oxygen Release Platform for Diabetic Wound Healing. *ACS Nano* *16*, 7486–7502. <https://doi.org/10.1021/acsnano.1c10575>.
39. Wu, Y., Li, Y., Liu, Y., Zhu, D., Xing, S., Lambert, N., Weisbecker, H., Liu, S., Davis, B., Zhang, L., et al. (2024). Orbit symmetry breaking in MXene implements enhanced soft bioelectronic implants. *Sci. Adv.* *10*, eadp8866. <https://doi.org/10.1126/sciadv.adp8866>.
40. Ju, X., Kong, J., Qi, G., Hou, S., Diao, X., Dong, S., and Jin, Y. (2024). A wearable electrostimulation-augmented ionic-gel photothermal patch doped with MXene for skin tumor treatment. *Nat. Commun.* *15*, 762. <https://doi.org/10.1038/s41467-024-45070-z>.
41. Li, Z., Zhang, H., Han, J., Chen, Y., Lin, H., and Yang, T. (2018). Surface Nanopore Engineering of 2D MXenes for Targeted and Synergistic Multi-therapies of Hepatocellular Carcinoma. *Adv. Mater.* *30*, 1706981. <https://doi.org/10.1002/adma.201706981>.
42. Li, J., Li, Z., Liu, X., Li, C., Zheng, Y., Yeung, K.W.K., Cui, Z., Liang, Y., Zhu, S., Hu, W., et al. (2021). Interfacial engineering of Bi₂S₃/Ti₃C₂T_x MXene based on work function for rapid photo-excited bacteria-killing. *Nat. Commun.* *12*, 1224. <https://doi.org/10.1038/s41467-021-21435-6>.
43. Wan, S., Chen, Y., Huang, C., Huang, Z., Liang, C., Deng, X., and Cheng, Q. (2024). Scalable ultrastrong MXene films with superior osteogenesis. *Nature* *634*, 1103–1110. <https://doi.org/10.1038/s41586-024-08067-8>.
44. Li, X., Huang, Z., Shuck, C.E., Liang, G., Gogotsi, Y., and Zhi, C. (2022). MXene chemistry, electrochemistry and energy storage applications. *Nat. Rev. Chem* *6*, 389–404. <https://doi.org/10.1038/s41570-022-00384-8>.
45. Simon, P., and Gogotsi, Y. (2008). Materials for electrochemical capacitors. *Nat. Mater.* *7*, 845–854. <https://doi.org/10.1038/nmat2297>.
46. Zhou, H., Zhao, Y., Zha, X., Zhang, Z., Zhang, L., Wu, Y., Ren, R., Zhao, Z., Yang, W., and Zhao, L. (2024). A Janus, robust, biodegradable bacterial cellulose/Ti₃C₂T_x MXene bilayer membranes for guided bone regeneration. *Biomater. Adv.* *167*, 213892. <https://doi.org/10.1016/j.bioadv.2024.213892>.
47. Li, C., Guo, C., Fitzpatrick, V., Ibrahim, A., Zwierstra, M.J., Hanna, P., Lechtig, A., Nazarian, A., Lin, S.J., and Kaplan, D.L. (2019). Design of biodegradable, implantable devices towards clinical translation. *Nat. Rev. Mater.* *5*, 61–81. <https://doi.org/10.1038/s41578-019-0150-z>.
48. Lee, G., Ray, E., Yoon, H.-J., Genovese, S., Choi, Y.S., Lee, M.-K., Şahin, S., Yan, Y., Ahn, H.-Y., Bandodkar, A.J., et al. (2022). A bioresorbable peripheral nerve stimulator for electronic pain block. *Sci. Adv.* *8*, eabp9169. <https://doi.org/10.1126/sciadv.abp9169>.
49. Choi, Y.S., Hsueh, Y.-Y., Koo, J., Yang, Q., Avila, R., Hu, B., Xie, Z., Lee, G., Ning, Z., Liu, C., et al. (2020). Stretchable, dynamic covalent polymers for soft, long-lived bioresorbable electronic stimulators designed to facilitate neuromuscular regeneration. *Nat. Commun.* *11*, 5990. <https://doi.org/10.1038/s41467-020-19660-6>.
50. Vey, E., Rodger, C., Meehan, L., Booth, J., Claybourn, M., Miller, A.F., and Saiani, A. (2012). The impact of chemical composition on the degradation kinetics of poly(lactic-co-glycolic) acid copolymers cast films in phosphate buffer solution. *Polym. Degrad. Stabil.* *97*, 358–365. <https://doi.org/10.1016/j.polymdegradstab.2011.12.010>.
51. Luo, Y., Que, W., Tang, Y., Kang, Y., Bin, X., Wu, Z., Yuliarto, B., Gao, B., Henzie, J., and Yamauchi, Y. (2024). Regulating Functional Groups Enhances the Performance of Flexible Microporous MXene/Bacterial Cellulose Electrodes in Supercapacitors. *ACS Nano* *18*, 11675–11687. <https://doi.org/10.1021/acsnano.3c11547>.
52. Yeom, J., Choe, A., Lee, J., Kim, J., Kim, J., Oh, S.H., Park, C., Na, S., Shin, Y.-E., Lee, Y., et al. (2023). Photosensitive ion channels in layered MXene membranes modified with plasmonic gold nanostars and cellulose nanofibers. *Nat. Commun.* *14*, 359. <https://doi.org/10.1038/s41467-023-36039-5>.
53. Guimarães, C.F., Gasperini, L., Marques, A.P., and Reis, R.L. (2020). The stiffness of living tissues and its implications for tissue engineering. *Nat. Rev. Mater.* *5*, 351–370. <https://doi.org/10.1038/s41578-019-0169-1>.
54. Wang, X., Salari, M., Jiang, D.-e., Chapman Varela, J., Anasori, B., Wesolowski, D.J., Dai, S., Grinstaff, M.W., and Gogotsi, Y. (2020). Electrode material–ionic liquid coupling for electrochemical energy storage. *Nat. Rev. Mater.* *5*, 787–808. <https://doi.org/10.1038/s41578-020-0218-9>.
55. Wu, S., Hua, M., Alsaied, Y., Du, Y., Ma, Y., Zhao, Y., Lo, C.-Y., Wang, C., Wu, D., Yao, B., et al. (2021). Poly(vinyl alcohol) Hydrogels with Broad-Range Tunable Mechanical Properties via the Hofmeister Effect. *Adv. Mater.* *33*, 2007829. <https://doi.org/10.1002/adma.202007829>.
56. Bae, J., Song, M.K., Park, Y.J., Kim, J.M., Liu, M., and Wang, Z.L. (2011). Fiber Supercapacitors Made of Nanowire-Fiber Hybrid Structures for Wearable/Flexible Energy Storage. *Angew Chem. Int. Ed. Engl.* *50*, 1683–1687. <https://doi.org/10.1002/anie.201006062>.
57. Lee, H., Lee, G., Yun, J., Keum, K., Hong, S.Y., Song, C., Kim, J.W., Lee, J.H., Oh, S.Y., Kim, D.S., et al. (2019). Facile fabrication of a fully biodegradable and stretchable serpentine-shaped wire supercapacitor. *Chem. Eng. J.* *366*, 62–71. <https://doi.org/10.1016/j.cej.2019.02.076>.
58. Lv, Q., Li, X., Tian, X., Fu, D.-a., Liu, H., Liu, J., Song, Y., Cai, B., Wang, J., Su, Q., et al. (2023). A Degradable and Biocompatible Supercapacitor Implant Based on Functional Sericin Hydrogel Electrode. *Adv. Energy Mater.* *13*, 2203814. <https://doi.org/10.1002/aenm.202203814>.
59. Tian, W., Li, Y., Zhou, J., Wang, T., Zhang, R., Cao, J., Luo, M., Li, N., Zhang, N., Gong, H., et al. (2021). Implantable and Biodegradable Micro-Supercapacitor Based on a Superassembled Three-Dimensional Network Zn@PPy Hybrid Electrode. *ACS Appl. Mater. Interfaces* *13*, 8285–8293. <https://doi.org/10.1021/acsmi.0c19740>.
60. Dubal, D.P., Aradilla, D., Bidan, G., Gentile, P., Schubert, T.J.S., Wimberg, J., Sadiq, S., and Gomez-Romero, P. (2015). 3D hierarchical assembly of ultrathin MnO₂ nanoflakes on silicon nanowires for high performance micro-supercapacitors in Li-doped ionic liquid. *Sci. Rep.* *5*, 9771. <https://doi.org/10.1038/srep09771>.
61. Sim, H.J., Choi, C., Lee, D.Y., Kim, H., Yun, J.-H., Kim, J.M., Kang, T.M., Ovalle, R., Baughman, R.H., Kee, C.W., and Kim, S.J. (2018). Biomolecule based fiber supercapacitor for implantable device. *Nano Energy* *47*, 385–392. <https://doi.org/10.1016/j.nanoen.2018.03.011>.
62. Yamada, S. (2022). A Transient Supercapacitor with a Water-Dissolvable Ionic Gel for Sustainable Electronics. *ACS Appl. Mater. Interfaces* *14*, 26595–26603. <https://doi.org/10.1021/acsmi.2c00915>.
63. Shao, M., Sheng, H., Lin, L., Ma, H., Wang, Q., Yuan, J., Zhang, X., Chen, G., Li, W., Su, Q., et al. (2023). High-Performance Biodegradable Energy Storage Devices Enabled by Heterostructured MoO₃–MoS₂ Composites. *Small* *19*, 2205529. <https://doi.org/10.1002/sml.202205529>.
64. Zhang, C.J., Pinilla, S., McEvoy, N., Cullen, C.P., Anasori, B., Long, E., Park, S.-H., Seral-Ascaso, A., Shmeliov, A., Krishnan, D., et al. (2017). Oxidation Stability of Colloidal Two-Dimensional Titanium Carbides (MXenes). *Chem. Mater.* *29*, 4848–4856. <https://doi.org/10.1021/acschemmater.7b00745>.
65. Persson, I., Halim, J., Hansen, T.W., Wagner, J.B., Darakchieva, V., Pališaitis, J., Rosen, J., and Persson, P.O.Å. (2020). How Much Oxygen Can a MXene Surface Take Before It Breaks? *Adv. Funct. Mater.* *30*, 1909005. <https://doi.org/10.1002/adfm.201909005>.